Biosensors and Bioelectronics 68 (2015) 570–576

Contents lists available at ScienceDirect

Biosensors and Bioelectronics

journal homepage: www.elsevier.com/locate/bios

A surface-acoustic-wave-based cantilever bio-sensor

Giorgio De Simoni [a,*], Giovanni Signore [a], Matteo Agostini [a,b], Fabio Beltram [b], Vincenzo Piazza [a]

[a] Center for Nanotechnology Innovation @NEST, Istituto Italiano di Tecnologia, Piazza San Silvestro 12, I-56127 Pisa, Italy
[b] NEST, Scuola Normale Superiore, Piazza San Silvestro 12, I-56127 Pisa, Italy

ARTICLE INFO

Article history:
Received 27 August 2014
Received in revised form
13 November 2014
Accepted 27 December 2014
Available online 30 December 2014

Keywords:
Cantilever bio-sensor
Surface acoustic wave

ABSTRACT

A scalable surface-acoustic-wave- (SAW-) based cantilevered device for portable bio-chemical sensing applications is presented. Even in the current, proof-of-principle implementation this architecture is shown to outperform commercial quartz–crystal microbalances in terms of sensitivity. Adhesion of analytes on a functionalized surface of the cantilever shifts the resonant frequency of a SAW-generating transducer due to the stress-induced variation of the speed of surface acoustic modes. We discuss the relevance of this approach for diagnostics applications based on miniaturized devices.

© 2015 Elsevier B.V. All rights reserved.

1. Introduction

Micro-electro-mechanical systems can provide ideal actuation and detection platforms for bio-chemical sensing applications. In particular, techniques derived from atomic force microscopy have attracted growing interest in the last 10 years. Microcantilevers were used as effective tools for a wide range of sensing applications in chemistry and life sciences and a number of reports exist on very sensitive cantilever-based assays for a multitude of analytes such as DNA (Fritz, 2000; Hansen et al., 2001; McKendry et al., 2002; Mukhopadhyay et al., 2005; Su et al., 2003; Zhang et al., 2006; Ndieyira et al., 2008), antigens, proteins, bacteria, pathogens (Arntz et al., 2003; Campbell et al., 2007; Gupta et al., 2004; Lee et al., 2005; Maraldo and Mutharasan, 2007; Wee et al., 2005), and ions (Ji and Thundat, 2002; Ji et al., 2000). Moreover, artificial noses (Baller et al., 2000), sensors for temperature change (Huang et al., 2008; Barnes et al., 1994; Berger et al., 1996), for infrared detection (Huang et al., 2008; Ivanova et al., 2005) and identification of explosives (Gilda et al., 2011; Pinnaduwage et al., 2003a,b; Senesac and Thundat, 2008; van Neste et al., 2008) were demonstrated. The success of this approach stems from its allowing label-free detection of the molecules of interest. Moreover, the size of these devices makes it possible to fabricate high-density parallel devices for high-throughput analysis.

Analyte recognition is usually achieved by coating one side of the cantilever with molecules that can selectively immobilize a target moiety. The so-called static operation mode is the most common approach for bio-sensing experiments: adsorption of molecules leads to mechanical stress on the cantilever surface which in turn leads to a deflection of the device. In the dynamic mode, in turn, cantilevers are excited close to one of their resonance frequencies: when additional mass attaches to the oscillating cantilever, the resonance frequency of the latter lowers, so that a precise measurement of the loaded mass can be obtained after a suitable calibration. It was demonstrated that, with optimized cantilever geometries and under ultra-high vacuum, it is possible to detect mass changes down to the single molecule limit (Yang et al., 2000).

The usual technique to measure the response of a cantilever exploits laser-light reflection off its surface. The reflected beam is collected by a position-sensitive detector, which provides an electrical signal proportional to the deflection of the cantilever via optical-lever amplification. This method affords high sensitivity (in the sub-nm deflection range), but requires optical alignment of space consuming setups, therefore severely limiting the exploitation of such technology in real-life lab-on-chip architectures. Other common methods exploit direct transduction of the cantilever deflection into an electrical signal through piezo-resistive or piezoelectric levers. The latter approaches have the advantage of full on-chip integrability, thanks to the direct electric readout of the deflection and are the technique of choice for detector arrays. On the other hand they yield significantly lower sensitivity with respect to optical methods.

2. Surface acoustic wave driven cantilever sensors

Here we demonstrate a method to realize a cantilever sensor in which surface stress due to molecular binding on the beam surface

* Corresponding author.
E-mail address: giorgio.desimoni@iit.it (G. De Simoni).

http://dx.doi.org/10.1016/j.bios.2014.12.058
0956-5663/© 2015 Elsevier B.V. All rights reserved.

is read through an interdigitated transducer (IDT) fabricated on the lever surface (Strambini et al., 2010). This approach is compatible both with static and dynamic operation modes. Importantly it can be exploited also with passive wireless readout schemes (Cole and Vaughn, 1972; Huang et al., 2010). As a result, it is very appealing in view of the implementation of scalable devices for diagnostic purposes.

Devices consist of a micro-cantilever made of a piezoelectric 2.5-μm – thick GaAs/AlAs membrane that is fabricated starting from a molecular-beam-epitaxy-grown heterostructure by removing the GaAs substrate via selective etching. The thickness of the membrane was set to 2.5 times the chosen SAW wavelength (1 μm) in order to avoid bulk resonances. The bottom surface of the membrane was coated with a 10-nm-thick gold layer. This surface is then functionalized to fabricate the sensing area of the device. An IDT is present on the top surface. The IDT is a comb-shaped metallic (50-nm thick Al layer, in the present implementation) periodic structure that can resonantly transduce an RF signal into a surface acoustic wave (SAW) traveling on the piezoelectric substrate.

The IDT resonance frequency f_0 is given by

$$f_0 = \frac{v}{\lambda}, \tag{1}$$

where v is the velocity of the excited surface acoustic mode and λ is the spatial periodicity of the IDT. f_0 can be experimentally determined by measuring the fraction of the excitation power reflected by the IDT as a function of frequency: the minimum in the reflection spectrum corresponds to maximum energy transfer into the acoustic mode. Fig. 1 shows a scheme of the device and measurement setup together with images of a representative device.

This device geometry was initially proposed by Strambini et al. (2010) as an all-electrical cantilever for atomic-force microscopy. In that implementation, a longitudinal bending of the cantilever was induced by pushing its free edge with a rigid tip controlled by a calibrated piezo-translator, leading to a variation of the periodicity of the IDT and consequently of its resonance frequency with sensitivity $s = \Delta f L/\Delta z$ (where L is cantilever length and Δz is vertical displacement of its tip) of the order of 1 MHz. Here we show that surface stress acting on the cantilever *bottom* surface (as a result of analyte adsorption on the functionalized area) can lead to a dramatically enhanced sensitivity that cannot be explained only in terms of variation of IDT periodicity but relies on the presence of stress distributed through the whole cantilever body. We demonstrate that this mechanism can be exploited for biosensing applications by a thiol-modified-biotin/streptavidin binding recognition experiment.

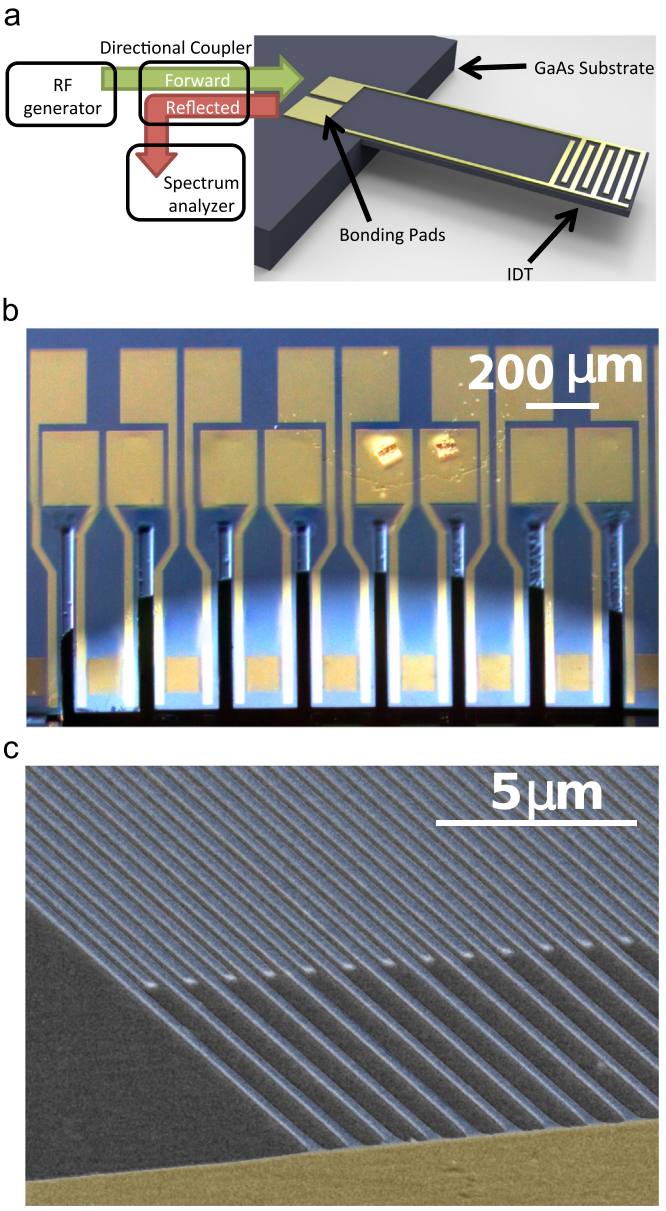

Fig. 1. (a) Scheme of the device and of the measurement setup. Power reflected by the IDT as a function of frequency is measured by a spectrum analyzer. (b) Top-view of a representative device. (c) A detail of an IDT: false color picture obtained by a scanning-electron-microscope. Blue electrode correspond to IDT fingers, yellow area is a section of a RF bus-bar. (For interpretation of the references to color in this figure caption, the reader is referred to the web version of this paper.)

3. On-chip measurement of biotin–streptavidin interaction

In order to test the performance of the present cantilevered devices as surface-stress sensors for biochemical applications, we chose the biotin–streptavidin pair as benchmark for molecular-recognition events. To this end the metallized side of the cantilever was coated with a thiol-modified biotin (TB) and the IDT resonance shift was measured following biotin–streptavidin interaction. Each device was characterized by acquiring its unstressed spectrum, *i.e.* before it was exposed to the TB. Devices were wetted with 20 μL of TB dissolved in degassed water/ethanol (9/1 v/v) solutions at a concentration of 1 mg/mL for 10 min without stirring. The sample was then washed with MilliQ-grade water, and dried. After such dip-wash-dry procedure the IDT resonance frequency was measured again. Due to the formation of gold–thiol chemical bonds, the IDT resonance was observed to red-shift, with $\Delta f/f_0$ of the order of 10^{-3}. We should like to underline that such a frequency shift would require a cantilever vertical deflection of the order of 100 μm for a device with the sensitivity reported in Strambini et al. (2010). On the contrary, optical profilometry measurements demonstrate that our devices undergo a vertical deflection which is below or comparable with instrumental accuracy (~30 nm). Moreover, our device is not expected to show any sensitivity to mass-loading, since the analytes are immobilized at the bottom surface of the cantilever beam, which is not probed by the SAW. In light of these considerations, in this measurement configuration, any effect directly related with IDT periodicity variation or with mass-loading can be regarded as negligible. On the other hand SAW-based cantilever devices show an enhanced sensitivity to the stress applied in the volume of material in which the SAW is generated, *i.e.* just beneath the IDT.

The origin of this effect is likely to be found in the presence of residual stress in the beam body, which is introduced during the cantilever fabrication procedure. The residual stress is then tuned by the surface stress induced by molecule adhesion and acts as an amplifier of stress sensitivity, as discussed in *Finite element device modeling* section of this paper. To get a confirmation of this hypothesis, we performed TB-binding control experiments on bulk SAW-devices, comprising of a 50-nm-thick gold IDT. Device frequency shift due to TB adhesion directly on the IDT free surface, was measured following the same protocol used for cantilevered devices. In this configuration, $\Delta f/f_0$ was always $\lesssim 5\times10^{-5}$. This fact confirms the role of the specific configuration of the stress in a cantilever beam in producing an amplification of the stress signal detected by the IDT.

The ability of the SAW-based cantilevered devices to detect TB-streptavidin binding was probed by wetting TB-coated devices with streptavidin/water solutions with molar concentration $[S]$ ranging between 4 pM and 80 μM. Devices were left without stirring for 10 min in contact with 20 μL of each solution, then washed with water and dried. The resonance frequency was then measured again. For $[S]$ below ~10 nM IDT resonance frequency oscillates around the biotin-covered device resonance frequency. Such behavior is due to the handling steps involved in the dip–wash–dry–measure procedure which introduces a noise (or device instability) of the order of 100 kHz in the determination of resonance frequency of the IDT (resulting in a relative frequency resolution for the whole procedure $\delta f/f \sim 1\times10^{-4}$). When $[S] \gtrsim 10$ nM, the IDT resonance initially decreases with streptavidin concentration as a power law and finally saturates at ~2 times the shift produced by the initial TB–gold binding for $[S] \gtrsim 4$ μM. Sample cleaning with an oxygen-plasma brings the IDT resonance frequency back to its original value. Fig. 2a reports the IDT spectra of a representative device before and after exposure to TB and streptavidin solutions at different concentrations. Fig. 2b shows a scatter plot of the relative frequency shift of the same device as function of $[S]$. A likely origin of the threshold behavior of our devices lies in the collective nature of the stress-transduction mechanism. It requires a relatively large fraction of the TB sites to be occupied by streptavidin in order to make short-range steric repulsion capable of yielding a surface stress distributed on the whole cantilever active area. In this picture, similarly to what proposed in Ndieyira et al. (2008), it is possible to express the relative frequency shift as a function of the fraction p of occupied TB sites:

$$\frac{\Delta f}{f_0} = \delta_{TB} + \gamma\theta_h(p-pc)\left(\frac{p-p_c}{1-p_c}\right)^{\beta} \tag{2}$$

where p_c is a percolation threshold beyond which streptavidin clusters are large enough to produce macroscopic bending of the cantilever, $\theta_h(p-p_c)$ is the Heaviside step function, β describes the interaction between chemically reacted regions on the cantilever and the stress/frequency-shift transduction mechanism, δ_{TB} is the offset shift resulting from TB–gold adhesion, and the constant γ corresponds to the maximum surface stress (and resonance shift) occurring when all accessible sites are occupied. p is a function of streptavidin concentration and can be determined through the equilibrium association constant K_A by means of the Langmuir adsorption isotherm:

$$p = \frac{K_A[S]}{1+K_A[S]}. \tag{3}$$

These relations highlight the collective nature of surface stress: when only a small fraction of the available TB sites is occupied (*i.e.* $p \ll p_c$) no macroscopic stress is produced, when $p \gtrsim p_c$ any further increase in streptavidin concentration results in an increased

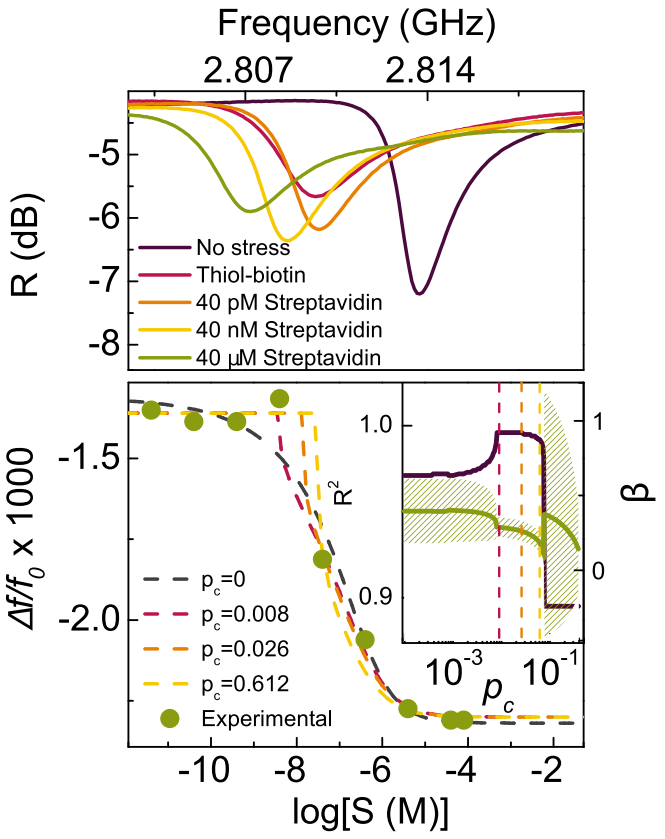

Fig. 2. (a) IDT spectra of a representative device before being exposed to analytes, after gold–TB and biotin–streptavidin (several concentrations) bindings. (b) Scatter plot of the relative frequency shift $\Delta f/f_0$ of the same device of panel (a) as a function of streptavidin concentration $[S]$, where f_0 is the frequency of the unstressed device. Dashed lines are the result of best fitting procedures of experimental data points with the Langumuir-percolation model presented in the paper for $p_c = 0$, $p_c = 0.008$ (purple), $p_c = 0.026$ (orange) and $p_c = 0.061$ (yellow). (c) Fit coefficient of determination R^2 as a function of p_c (purple curve) and concomitant evolution of β (green curve). Green-shaded area correspond to 95%-confidence bounds for β. Dashed vertical lines correspond to p_c values of curves plotted in panel (b). (For interpretation of the references to color in this figure caption, the reader is referred to the web version of this paper.)

average cluster size which leads to an enhanced surface stress. For steric first-neighbor interaction p_c must be finite and is determined by the geometric properties of the host site lattice. As the length scale of the interaction grows, p_c is expected to tend to zero. It is worth noting that, in this picture, for $p < p_c$ the device is effectively *blind* and that, given the functionalization layer and the analyte, p_c somehow provide a fundamental detection limit. Nonetheless, we stress that in our experiment we were able to detect TB–streptavidin binding at $[S] \sim 10$ nM, which is 10 times lower than the minimum concentration detectable with a typical QCM-D setup (see Appendix D). Moreover such value is consistent with the detection threshold of streptavidin–biotin binding reported for cantilevered sensor with optical deflection readout (Shu et al., 2007). In order to ascertain the validity of the proposed percolation model, we have carried out a series of least-squares fits of Eq. (2) to our data, with K_A set equal to $2\times10^6\ \mathrm{M}^{-1}$ as determined through a QCM-D (see Appendix D). As already highlighted in Ndieyira et al. (2008) the parameters β and p_c are statistically coupled. Therefore, to determine their best values, we examined directly how the fit changes as a function of p_c, looking at the coefficient of determination R^2. Fig. 2c reports the coefficient of determination R^2 (purple line) as function of p_c. Increasing p_c from 0 to 1, R^2 quickly approach one, reaching its maximum (0.996) for $p_c = 0.008$. It remains constant up to $p_c = 0.026$ and

then slightly decreases down to $p_c = 0.061$ ($R^2 = 0.992$). Above such value R^2 drops to 0.9 and below. Dashed curves in Fig. 2b are the result of the best-fitting procedures of experimental data for $p_c = 0.008$, $p_c = 0.026$ and $p_c = 0.061$. The fitting procedures yielded in all the three cases $\delta_{TB} \sim -1.3 \times 10^{-3}$ and $\gamma \sim -9 \times 10^{-4}$, while β ranges between ~0.3 and ~0.2. Fig. 2c shows (green line) the behavior of β as a function of p_c. This analysis confirms the existence of a finite percolation threshold comprised in the interval 0.008–0.061, corresponding to $[S] = 4$–30 nM.

4. Tuning the surface stress through the pH of the solution

In order to further verify that surface stress is the driving mechanism of the observed IDT-resonance frequency shift, cantilever surface stress was modulated through protonation/deprotonation of the adsorbed molecules. In this case mass-loading effects are negligible since the deposited mass essentially does not change during the experiment, except for a minor contribution by the counter ions arising from the volatile buffer employed. Samples were immersed for 30 min in an aqueous solution containing cysteine 10 mM, whose pH had been adjusted at 6.00. Note that the isoelectric point for cysteine is 6.02 so that electrostatic repulsion between adsorbed cysteine residues is minimal at this pH. The sample was washed with water, dried, and its resonance frequency was measured. Following cysteine binding on the gold surface, IDT resonance was observed to red shift, with $\Delta f/f_0$ of the order of 10^{-3}. The sample was then inserted in an acidic buffer (ammonium acetate 100 mM, pH 5.01), dried under vacuum, and its resonance frequency was measured again. At acidic pH, the cysteine residues become positively charged, owing to the protonation of both the carboxylic residue and of the amino functional group. The electrostatic repulsion is only partially shielded by the volatile counter ion and since, as mentioned above, mass increase is negligible, the observed additional resonance red-shift must stem from the increased Coulomb repulsion and from the surface stress it produces. Finally, the sample was inserted in a buffer at pH 6.00 (ammonium acetate 100 mM), dried under high vacuum, and its resonance frequency was measured again. When the cysteine residues are inserted in a medium at pH 6.00, *i.e.* at their isoelectric point, no net charge is present on the surface of the amino acidic coating of the cantilever, since there is a complete balance of positive and negative charges on each amino acid. Furthermore, the volatile buffer is completely removed under vacuum, thus eliminating any mass loading effect. This would ultimately result in a coating identical to that obtained with the dip in the first cysteine solution. Indeed, the additional surface stress introduced by amino acid protonation is removed and IDT resonance returns to the previously measured value. Table 1 reports the IDT frequency shifts of a representative device after cysteine adhesion, at pH 5.01 and pH 6.00. Data confirm that surface stress is the mechanism at the origin of the observed IDT resonance shifts. Indeed this effect can be modulated by changing the charge properties of the adsorbed mono-layer without affecting its mass.

Table 1
Relative frequency shift of a representative device in correspondence to different pH values.

Solution description	pH	$\frac{\Delta f}{f_0} \times 10^{-5}$
10 mM cysteine aqueous solution	6.0	174 ± 5
100 mM ammonium acetate acidic buffer	5.01	248 ± 5
100 mM ammonium acetate buffer	6.0	195.3 ± 0.5

5. Finite element device modeling

The effect of residual and surface stress on the stiffness of cantilever beams is a subject of intense debate and remains a rather open issue, but several experimental studies report a significant stiffness change due to surface stress (see, *e.g.*, Karabalin et al., 2012 and referenced within). Since IDT resonance frequency is, through sound velocity, a function of the mass density and of the stiffness tensor of the material in the regions directly probed by the SAW, it is not surprising that the distribution of the stress is crucial in determining the behavior of this class of devices. In order to better understand the origin of IDT-frequency shifts induced by molecule adhesion on the active area of the device, a prototypical device was modeled by means of a 3-dimensional (3D) finite-element calculation which allowed us to simulate SAWs propagating along the (1 1 0) axis (from now on *x*-axis, see Fig. 3) of a 2.5 μm – thick slab cut out from a (0 0 1) (from now on *z*-axis, the third axis is the *y*-axis, see Fig. 3) GaAs substrate.

The simulated device comprises 15 periods of a 50% filling-fraction 1-μm – period aluminum IDT for SAW generation and gold RF bus-bars. Two acoustic-dampers (blue blocks in the inset of Fig. 3) were added in order to avoid reflections of the wave at the edges of the simulation domain. At the very bottom of the domain a 50-nm-thick layer (green block in inset of Fig. 3, from now on the *stressing* layer) can be mass-loaded and expanded or contracted to mimic mass-loading and surface-stress effects due to molecule adhesion on the cantilever bottom face. IDT-resonance frequency shift was calculated by a three-step procedure. The distribution of residual stress (τ_{ij}) is not accessible experimentally and it is not known *a priori*. On the other hand, optical profilometry measurements on actual devices showed that cantilevers are bent upward almost exclusively in the IDT region, meaning that the most relevant part of the residual stress arises at the interface between electrode metal and substrate surface. For these reasons the distribution of intrinsic stress within the cantilever body was included indirectly in the FEM model in the first step of our simulations through an additional arbitrary term ϵ_r in the elastic equation:

$$s(x, y, z) - s_0(x, y, z) = c(\epsilon(x, y, z) - \epsilon_0(x, y, z) - \epsilon_r(x, y, z)), \quad (4)$$

where s, s_0 and ϵ, ϵ_0 are respectively the actual and initial stress and strain tensors, c is the elasticity matrix. Geometric non-linearities are also taken into account in the model by including in the expression of the strain the second-order term of the displacement field $\mathbf{u}$:

$$\epsilon = \frac{1}{2}[(\nabla \mathbf{u})^T + \nabla \mathbf{u} + (\nabla \mathbf{u})^T \nabla \mathbf{u}]. \quad (5)$$

Since, in our case, intrinsic stress is mainly due to metal deposition on the device surface, ϵ_r was set equal to 0 everywhere, except within the electrode domains. Moreover, it was assumed to be diagonal with equal *xx*, *yy*, *zz* components. This reduces the description of the intrinsic stress to a single parameter that drives an electrode contraction equivalent to an isotropic thermal shrink of the electrode material. This leads to a cantilever bent upwards around both *x* and *y* axes as experimentally observed in actual devices. Such description qualitatively gathers the main origin of intrinsic stress (and cantilever bending), which is likely to be found in the cooling of the hot metal vapor when it gets in contact with the cold GaAs surface. In the second step, in order to mimic the biaxial surface stress induced by molecule adhesion onto the bottom cantilever surface, an expansion was induced in the stressing layer alone by adding a constant term σ to the *xx* and *yy* components of its stress tensor (σ_{ij}). In this way we set the surface stress that acts on the bottom surface of the cantilever. A negative value of σ_{xx} and σ_{yy} corresponds to an expansion of the stressing

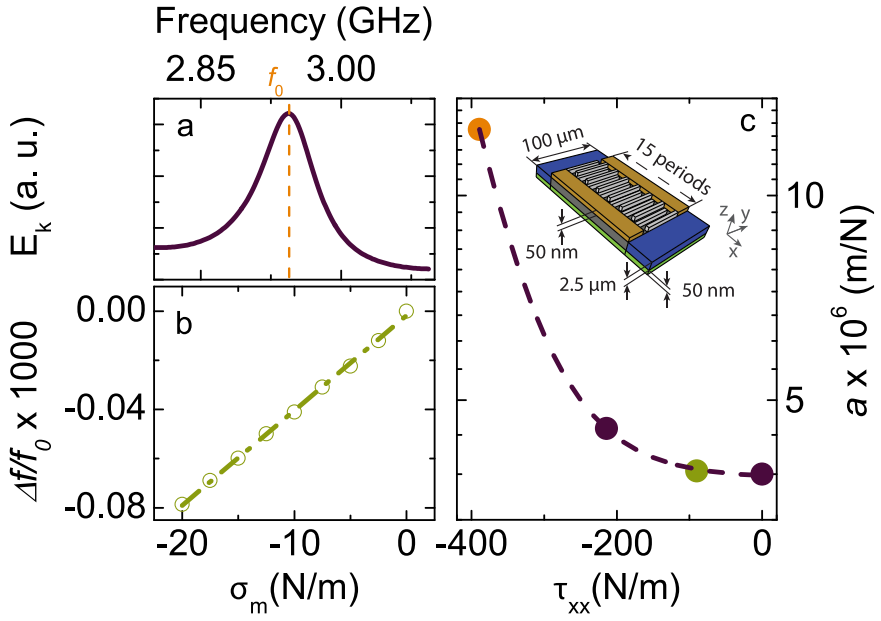

Fig. 3. (a) IDT spectrum for the unstressed cantilever. It is obtained calculating total kinetic energy as a function of the frequency of the IDT excitation signal. (b) IDT-resonance relative frequency shift as a function of surface stress and linear fit (dashed line) of the simulated points, for a release stress with *xx*, *yy* and *zz* components respectively equal to −90 N/m, yielding a curvature radius of 1.5 mm. Calculated slope is 11.5 kHz m/N. (c) Surface stress device sensitivity a as a function of the *xx* component of the residual stress τ. The green point corresponds to the same stress parameter of panel (b). Orange point corresponds to a device with the same sensitivity of actual devices. Inset: Geometrical details of the modeled device. The blue blocks are acoustic dampers avoiding SAW reflections at the edges of the simulation domain. The green layer is the stressing layer. (For interpretation of the references to color in this figure caption, the reader is referred to the web version of this paper.)

layer respectively along the x and y directions. In the last step, SAW propagation along the x-axis was simulated on the deformed domain resulting from the previous steps by applying a harmonic potential on one side of the IDT, while the other was kept at ground potential. At different intensities of τ (simulation step 1), simulations were performed for surface mass-loading values m between 0 and 400 ng/cm^2 and for biaxial surface stress σ ranging from 0 to −20 N/m (simulation step 2). The range of interest of m was defined by measuring the surface mass loading due to a complete covering of the device with TB and streptavidin monolayers by means of a quartz crystal micro-balance with dissipation (QCM-D) as reported in the Appendix D. The selected surface stress range is coherent with what reported in the literature (Fritz, 2008) for dodecanethiol in gas phase on gold, in light of the similar physico-chemical properties of the two systems (*i.e.* no net charge and hydrophobic behavior).

Simulation results showed that, $\Delta f = f(\sigma) - f(\sigma = 0)$ exhibits a linear dependence on surface stress, with negligible dependence on mass loading. The latter is a consequence of the fact that the added mass is on the lower cantilever surface, in a region that is not probed by the SAW. The slope a of $\Delta f/f_0$ *vs.* σ provides an estimation of the sensitivity of the device and was found to exhibit a super-linear growth as a function of the intensity of the residual stress (see Fig. 3). In particular, when the simulated cantilever is pre-stressed in order to have a curvature radius of about 1.5 mm (as usually measured by optical-profilometry in actual devices), $a \sim 4 \times 10^{-6}$ m/N. Such value is about 15 times lower than what expected basing on our biotin–gold binding experiments, nonetheless increasing the residual stress by about a factor of 5, a increases to match its expected value. The origin of such mismatch is likely to be found in an underestimation of the simulated residual stress, which we cannot directly measure on real devices and that is very difficult to quantitatively model owing to the complex structure of the substrate. These results can be qualitatively interpreted as follows: the total stress (Σ_{ij}) in the region beneath the IDT affects the stiffness of the material and therefore tunes the IDT resonance frequency. Σ_{ij} is given by the superposition of τ_{ij} and σ_{ij}. Since typically the residual stress is much higher than the biaxial surface stress induced by analyte adhesion, thanks to the non-linear characteristics of $f(\Sigma_{ij})$, the residual stress effectively acts as an amplifier of device surface-stress sensitivity. This fact results in a better sensitivity performance with respect to what could be obtained in residual-stress-free devices, such as conventional fixed or bulk SAW sensors. Fig. 3 reports the IDT spectrum for the unstressed device, Δf as a function of σ at $m = 0$ for a device stressed with a curvature radius of ~ 1.5 mm. Panel Fig. 3c reports a as a function of the *xx* component of the residual stress.

6. Conclusions

We demonstrated a novel SAW-based cantilever sensing architecture for bio-chemical applications. In the present proof-of-concept implementation, devices already outperform well-established method such as, for instance, QCM-D measurement technique. We demonstrated quantitative detection of streptavidin–biotin interaction. We believe that these results demonstrate the potential of this architecture for the realization of lab-on-chip systems and, in light of the compatibility of these devices with passive wireless readout schemes, their relevance for implantable in vivo biosensing applications.

Appendix A. Device fabrication procedure

Several devices were fabricated starting with a GaAs/AlAs heterostructure. Its composition is reported in Table A1.

The required processing steps are the following:

- Lift-off mask for 1-µm–periodicity and 100-period IDTs is defined on unprocessed sample surface by means of an electron-beam lithographic procedure. Thermal evaporation of 50 nm of Al follows. RF-bus bar and bonding pads for electrical wiring are realized by an optical lithographic procedure and thermal

Table A1
Composition of the heterostructure used for device production.

Layer	Thickness (nm)	Material
Beam layer	2000	GaAs
Superlattice stop layer	50/50 × 5	AlAs/GaAs
Buffer	200	GaAs
Substrate	500 000	GaAs

evaporation of 10/90/5 nm respectively of Cr, Au and Al.

- A membrane is defined by etching the sample from its bottom side. This procedure is performed by a selective citric acid wet-etching solution which removes substrate and buffer layers, but is ineffective on the stop layer.
- Cantilevers with length varying from ~100 to ~300 μm are cut out from the membrane around each IDT by optical lithographic procedure and an inductively-coupled-plasma reactive-ion etching procedure.
- A 10-nm thick Au layer is thermally evaporated on the bottom surface of the cantilever.

Cantilever fabrication procedure is depicted in Fig. A1.

Appendix B. Reagents and instruments

All reagents were purchased from Sigma Aldrich unless otherwise stated, and used without further purification. Water used in all the experiments was of MilliQ grade. Streptavidin was purchased from IBA-go, and used as received. LC-MS analyses were performed on a Dionex Ultimate 3000 HPLC, equipped with automated fraction collector, PDA detector, and interfaced with an ABSciex 3200 Q-TRAP mass spectrometer, using water and trifluoracetic acid (TFA) 0.01% (solvent A)/ACN and TFA 0.01% (solvent B) as mobile phase. LC-MS analyses were performed on a Phenomenex Proteo column (4.6 × 250, particle size 5 μm, 90 A).

Appendix C. Synthesis of biotin-thiol

The synthesis of N-(2-mercaptoethyl)-5-((3aS,4S,6aR)-2-oxohexahydro-1H-thieno[3,4-d]imidazol-4-yl)pentanamide (biotin-thiol) was performed with a two-step procedure according to what previously reported (Lin et al., 2007; Lo Conte et al., 2010). In a typical experiment, biotin (0.4 mmol, 100 mg) was dissolved in N,N-dimethylformamide (DMF) (1.5 mL). N-Hydroxysuccinimide (NHS) (1.1 equiv, 0.44 mmol) and N-(3-dimethylaminopropyl)-ethyl-carbodiimide hydrochloride (EDC) (200 mg, 1.04 mmol) were subsequently added to the homogeneous solution, and the mixture was stirred at 22 °C for 12 h. Triethylamine (250 μL) and cystamine sulfate (50 mg, 0.5 equiv, 0.2 mmol) were added, and the reaction stirred at 22 °C for 12 h. Reaction progress was monitored by HPLC. When complete conversion was achieved, the solvent was removed at reduced pressure, and the residue was triturated with water and filtrated. Biotin disulfide (104 mg, 86% yield) was recovered as white solid. The product was dissolved in degassed DMF (1.25 mL). Triethylamine (0.1 mL) and dithiothreitol (150 mg, 0.97 mmol) were added to the solution, and the mixture was heated at 40 °C for 2 h. When complete conversion was observed (RP-HPLC), the solvent was removed at reduced pressure, and the crude product was triturated with acetone (5 mL). Pure biotin thiol (HPLC) was obtained in 65% yield (68 mg) after filtration. Mass spectra were in agreement with what previously reported.

Appendix D. Quartz crystal micro-balance with dissipation measurements

Quartz crystal Micro-balance analyses were performed on a QCM- D device (model Q-sense E4, Q-sense, Gothenburg, Sweden) on gold-plated QCM-D sensors, using freshly degassed (vacuum/ultrasound) solutions. Before each experiment, gold coated sensors were cleaned according to manufacturer instructions. Briefly, the sensors were treated with plasma/oxygen (100 W, 10 min), then soaked for 5 min in a 5:1:1 mixture of MilliQ water, ammonia

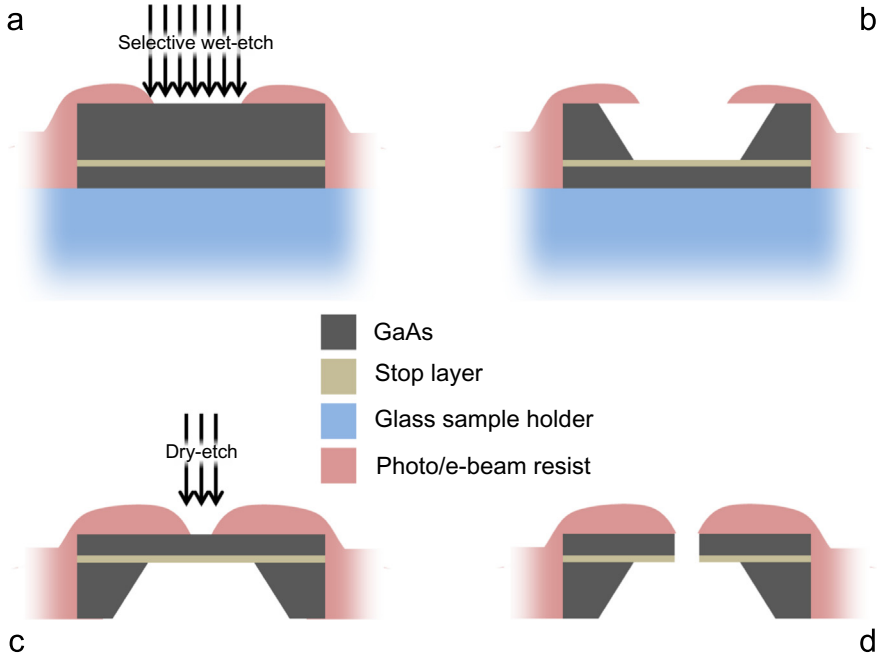

Fig. A1. Schematic of cantilever fabrication procedure. (a), (b) Device is mounted upside-down on a glass sample holder and a membrane is defined by optical lithography and wet-etching. (c), (d) Cantilever is released from the membrane by optical lithography and dry-etch procedure. After resist removal, the fabrication procedure is completed.

(25%) and hydrogen peroxide (30%) heated at 75 °C for 10 min, thoroughly washed with MilliQ water and with ethanol, and dried under gentle nitrogen flow. Then, sensors were treated again with plasma/oxygen (100 W, 10 min). In a typical experiment, the sensors were equilibrated with water at a flow of 0.1 mL/min until a stable baseline was achieved. Then, the sensors were subsequently treated with the following solutions (35 μL/min and 25 °C): (a) water/ethanol 9/1 v/v; (b) TB solution (1 mg/mL in water/ethanol 9/1 v/v); (c) water/ethanol 9/1 v/v; (d) water; (e) streptavidin solution; and (f) water. During each step, the flow was monitored until a stable baseline was observed. In a typical experiment, we measured a frequency shift of -8.9 ± 0.5 Hz upon adsorption of biotin-thiol, corresponding to a mass loading on the sensor surface of 158 ± 9 ng/cm^2. Dissipation change was negligible, in agreement with the formation of a stiff, ordered layer on sensor surface. When streptavidin solution was added to the sensor, a further frequency shift of -13.8 ± 0.3 Hz was observed, corresponding to a mass loading of 243 ± 6 ng/cm^2, and a negligible variation in dissipation, consistent with the formation of a disperse protein mono-layer on sensor surface.

Quantitative measurement of biotin–streptavidin binding constant was assessed as follows: after derivatization with biotin-thiol, the sensor was put in contact with increasing streptavidin concentrations (0.004–4000 nM, with 10-fold increments). In each step, frequency was monitored during 5 min. Resulting frequency shifts were well fitted with a Langmuir absorption isotherm. Fitting of the experimental data afforded a K_A of 2×10^6 M^{-1} $\pm$ 0.3×10^6.

References

Arntz, Y., Seelig, J.D., Lang, H.P., Zhang, J., Hunziker, P., Ramseyer, J.P., Meyer, E., Hegner, M., Gerber, C., 2003. Nanotechnology 14, 86–90.

Baller, M.K., Lang, P.H., Fritz, J., Gerber, C., Gimzewski, J.K., Drechsler, U., Rothuizen, H., Despont, M., Vettiger, P., Battiston, F.M., Ramseyer, J.P., Fornaro, P., Meyer, E., Güntherodt, H.-J., 2000. Ultramicroscopy 82, 1–9.

Barnes, J.R., Stephenson, R.J., Welland, M.E., Gerber, C., Gimzewski, J.K., 1994. Nature 372, 79.

Berger, R., Gerber, C., Gimzewski, J.K., Meyer, E., Güntherodt, H.J., 1996. Appl. Phys. Lett. 69, 40.

Campbell, G.A., Medina, M.B., Mutharasan, R., 2007. Sens. Actuators B: Chem. 126, 354–360.

Cole, P.H., Vaughn, R., 1972. Electronic Surveillance System.

Fritz, J., 2000. Science 288, 316–318.

Fritz, J., 2008. Analyst 133, 855–863. http://dx.doi.org/10.1039/b718174d.

Gilda N.A., Surya S., Joshi S., Thaker V., Baghini M. S., Sharma D. K., Rao V.R., 2011. In: International Conference on SoC Design (ISOCC), pp. 325–328.

Gupta, A., Akin, D., Bashir, R., 2004. Appl. Phys. Lett. 84, 1976.

Hansen, K.M., Ji, H.-F., Wu, G., Datar, R., Cote, R., Majumdar, A., Thundat, T., 2001. Anal. Chem. 73, 1567–1571.

Huang, S., Tao, H., Lin, I.-K., Zhang, X., 2008. Sens. Actuators A: Phys. 145–146, 231–240.

Huang, Y.-S., Chen, Y.-Y., Wu, T.-T., 2010. Nanotechnology 21, 095503.

Ivanova, K., Ivanov, T., Rangelow, I.W., 2005. J. Vac. Sci. Technol. B: Microelectron. Nanometer Struct. 23, 3153.

Ji, H., Thundat, T., 2002. Biosens. Bioelectron. 17, 337–343.

Ji, H.-F., Dabestani, R., Brown, G.M., Britt, P.F., 2000. Chem. Commun., 457–458.

Karabalin, R.B., Villanueva, L.G., Matheny, M.H., Sader, J.E., Roukes, M.L., 2012. Phys. Rev. Lett. 108, 236101.

Lee, J.H., Hwang, K.S., Park, J., Yoon, K.H., Yoon, D.S., Kim, T.S., 2005. Biosens. Bioelectron. 20, 2157–2162.

Lin, P.-C., Ueng, S.-H., Yu, S.-C., Jan, M.-D., Adak, A.K., Yu, C.-C., Lin, C.-C., 2007. Org. Lett. 9, 2131–2134.

Lo Conte, M., Pacifico, S., Chambery, A., Marra, A., Dondoni, A., 2010. J. Org. Chem. 75, 4644–4647.

Maraldo, D., Mutharasan, R., 2007. Anal. Chem. 79, 7636–7643.

McKendry, R., Zhang, J., Arntz, Y., Strunz, T., Hegner, M., Lang, H.P., Baller, M.K., Certa, U., Meyer, E., Güntherodt, H.-J., Gerber, C., 2002. Proc. Natl. Acad. Sci. USA 99, 9783–9788.

Mukhopadhyay, R., Lorentzen, M., Kjems, J., Besenbacher, F., 2005. Langmuir: ACS J. Surf. Colloids 21, 8400–8408.

Ndieyira, J.W., Watari, M., Barrera, A.D., Zhou, D., Vögtli, M., Batchelor, M., Cooper, M.A., Strunz, T., Horton, M.A., Abell, C., Rayment, T., Aeppli, G., McKendry, R.A., 2008. Nat. Nanotechnol. 3, 691–696.

Pinnaduwage, L.A., Boiadjiev, V., Hawk, J.E., Thundat, T., 2003a. Appl. Phys. Lett. 83, 1471.

Pinnaduwage, L.A., Gehl, A., Hedden, L., Muralidharan, G., Thundat, T., Lareau, R.T., Sulchek, T., Manning, L., Rogers, B., Jones, M., Adams, J.D., 2003b. Nature 425, 2003.

Senesac, L., Thundat, T., 2008. Mater. Today 11, 28–36.

Shu, W., Laue, E.D., Seshia, A.A., 2007. Biosens. Bioelectron. 22, 2003–2009.

Strambini, E., Piazza, V., Pingue, P., Biasiol, G., Sorba, L., Beltram, F., 2010. Appl. Phys. Lett. 96, 173505.

Su, M., Li, S., Dravid, V.P., 2003. Appl. Phys. Lett. 82, 3562.

van Neste, C.W., Senesac, L.R., Yi, D., Thundat, T., 2008. Appl. Phys. Lett. 92, 134102.

Wee, K.W., Kang, G.Y., Park, J., Kang, J.Y., Yoon, D.S., Park, J.H., Kim, T.S., 2005. Biosens. Bioelectron. 20, 1932–1938.

Yang, J., Ono, T., Esashi, M., 2000. Sens. Actuators A: Phys. 82, 102–107.

Zhang, J., Lang, H.P., Huber, F., Bietsch, a., Grange, W., Certa, U., McKendry, R., Güntherodt, H.-J., Hegner, M., Gerber, C., 2006. Nat. Nanotechnol. 1, 214–220.